Citation for published version:
Ma, C, Li, J, Zhang, N, Bu, F & Yang, Z 2022, 'Open-Circuit Radial Stray Magnetic Flux Density Based Non-invasive Diagnosis for Mixed Eccentricity Parameters of Interior Permanent Magnet Synchronous Motors in Electric Vehicles', *IEEE Transactions on Industrial Electronics*. https://doi.org/10.1109/TIE.2022.3165250

DOI:
10.1109/TIE.2022.3165250

Publication date:
2022

Document Version
Peer reviewed version

Open-Circuit Radial Stray Magnetic Flux Density Based Non-invasive Diagnosis for Mixed Eccentricity Parameters of Interior Permanent Magnet Synchronous Motors in Electric Vehicles

Conggan Ma, *Senior Member, IEEE*, Jiaming Li, Nic Zhang, Feifei Bu*, Senior Member, IEEE*,
Zhixin Yang*, Member, IEEE*

***Abstract*—By measuring the open-circuit radial stray magnetic flux density (RSMFD) of three spatial points, a novel diagnostic method for the eccentricity of interior permanent magnetic motors (IPMSMs) in electric vehicles (EVs) is proposed. Outperforming traditional methods, the proposed method can non-invasively diagnose not only the severities of static eccentricity (SE), dynamic eccentricity (DE), and mixed eccentricity (ME), but also the eccentricity location. In this paper, diagnosis results are described through three eccentricity parameters: SE ratio, DE ratio, and SE angle. Firstly, an analytical model of the open-circuit RSMFD of the IPMSM is proposed, with its accuracy validated by experiments. The pattern of the impact of the eccentricity parameters on the open-circuit RSMFD is analyzed to form the basis of the proposed method. Then, an eccentricity prototype motor, which can continuously emulate the eccentricity according to any listed eccentricity parameters, is developed. A test rig is built to collect the open-circuit RSMFD and validate the analytical calculation results. Finally, an eccentricity diagnostic model based on the open-circuit RSMFD is established. The diagnosis results proved the non-invasiveness, effectiveness, and viability of the proposed method.**

***Index Terms*—Air-gap eccentricity, permanent magnet motors, stray magnetic field, fault diagnosis, neural networks.**

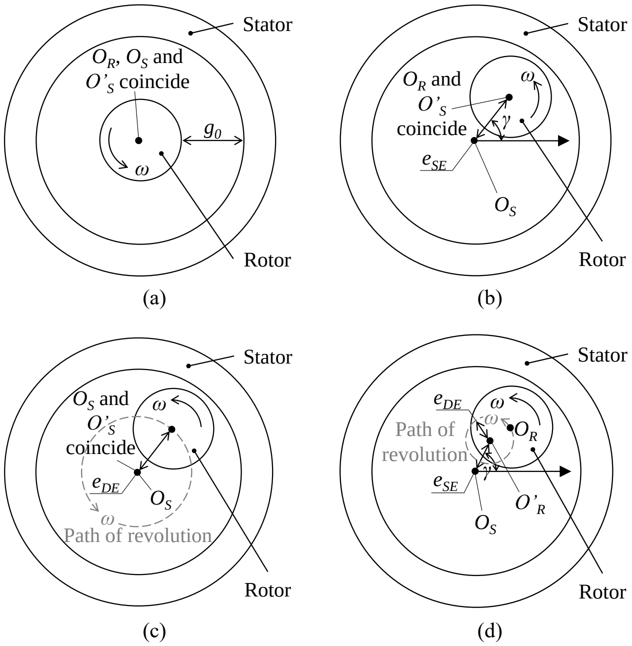

Fig. 1. Cross section of the motor. (a) no eccentricity. (b) static eccentricity. (c) dynamic eccentricity. (d) mixed eccentricity

I. INTRODUCTION

ECCENTRICITY of rotary motors is a phenomenon that the air gap is uneven due to a small offset between the geometric centers of the stator and the rotor. In general, an eccentricity ratio less than 10% is considered acceptable [1]. With a further increase of the eccentricity ratio, however, the unbalanced magnetic pull (UMP) also increases [2], resulting in the deterioration of the noise and vibration performance [3], [4]. Moreover, a severe eccentricity can even cause a fatal rotor-to-stator rub. Assuming that the outer outline of the rotor and the inner outline of the stator are ideal circles, there are three types of eccentricity to be investigated: static eccentricity (SE), dynamic eccentricity (DE), and mixed eccentricity (ME), as shown in Fig. 1, where O_S and O_R are geometric centers of the stator and the rotor, respectively. When DE or ME occurs, O_R revolves. Then, the path of the revolution of O_R is formed, whose center is O'_R. e_{SE} and e_{DE} are defined as the length of

---

Manuscript received September xx, 2021; revised Month xx, 2021; accepted Month xx, xxxx. This work was supported in part by National Natural Science Foundation of China under Grant 51975141 and Grant 51605112, in part by Natural Science Foundation of Shandong Province under Grant ZR2015EQ020, in part by the 2018 Open Fund of State Key Laboratory of Comprehensive Technology on Automobile Vibration and Noise & Safety Control under Grant 2018-03, and in part by the Science and Technology Development Fund, Macau (Grant no. 0018/2019/AKP, and SKL-IOTSC(UM)-2021-2023). *(Corresponding author: Jiaming Li.)*

Conggan Ma is with Harbin Institute of Technology-Weihai, Weihai, 264209, China (e-mail: mcg@hit.edu.cn).

Jiaming Li and Zhixin Yang are with State Key Laboratory of Internet of Things for Smart City and Department of Electromechanical Engineering, University of Macau, Macau SAR, China (email: yc17428@connect.um.edu.mo; zxyang@um.edu.mo).

Nic Zhang is with University of Bath, Bath, the UK (email: qz254@bath.ac.uk).

Feifei Bu is with Nanjing University of Aeronautics and Astronautics, Nanjing, China (e-mail: pufeifei@nuaa.edu.cn).

line segments $O_SO'_R$ and $O_RO'_R$, respectively. In this way, eccentricity can be described by three eccentricity parameters: SE ratio $\varepsilon_{SE} = e_{SE}/g_0$, DE ratio $\varepsilon_{DE} = e_{DE}/g_0$, and SE angle γ. ε_{SE} and ε_{DE} represent the severity of eccentricity, and γ represents the direction of SE. Measures like adding shims or modifying the bearing seat can be taken to reduce ε_{SE} if γ of the motor is known. Besides, as the rotor is gradually dragged to a more eccentric position because the direction of UMP is roughly consistent with γ [5], strengthening the structures of bearing seats or end-caps alongside γ may delay this bad trend. Due to manufacturing tolerance, bearing wear, structure deformation, etc., all motors exhibit a certain level of eccentricity, in which ME is the most common issue.

Traction motors for electric vehicles (EVs), are often designed as interior permanent magnet synchronous motors (IPMSMs) due to their high torque and power density, high efficiency, as well as strong flux weakening capability. These IPMSMs are designed with a narrow air gap (smaller than 1 mm) to reduce the open-circuit magnetic flux leakage, which consequently makes them more sensitive to eccentricity. Moreover, compared with surface-mounted permanent magnet synchronous motors, IPMSMs are prone to worse performance when eccentricity occurs due to magnetic saturation [6]. As a result, the eccentricity diagnosis for IPMSMs is an important topic in the context of the booming EV market.

Using additional sensors or original components of motors to obtain relevant signals, is a prerequisite of eccentricity diagnosis. Depending on the types of signals, existing eccentricity diagnostic methods are reviewed as follows:

(1) Air-gap magnetic field. When eccentricity occurs, air-gap magnetic flux density changes due to the variation of the air-gap length. Mirzaeva *et al.* [7], [8] obtained the data of air-gap magnetic flux density by placing 36 Hall sensors on the inner surface of the stator and then successfully diagnosed the eccentricity of a motor. As an invasive method, however, this method changes the structure of the original motor. Also, this method has to put a considerable number of expensive sensors in the air gap and is thus not suitable for traction motors for EVs, which are sensitive to cost as well as having a narrow air gap.

(2) Search coils (SCs) voltage. Due to the inconvenience of direct measurement of the air-gap magnetic field, the SCs voltage is often used instead. The SCs can be wound around either the armature teeth [9]–[12] or the stator yoke [13] or even made into PCBs and then mounted on the surface of the armature teeth [14]. Completely or partially derived from the air-gap magnetic field, the SCs voltage can be used as an informative indication of the eccentricity and gains popularity as an effective method. Unfortunately, this method is not suitable to be extensively applied in traction motors for EVs also due to its invasive nature.

(3) Stator current or back electromotive force (EMF). In comparison, using stator current or back EMF to diagnose the eccentricity of induction motors is convenient, effective, and non-invasive [1], [15]. However, most traction IPMSMs for EVs have multiple unit motors (≥3) to meet the needs for high torque at low speed. Moreover, these IPMSMs are also rotational symmetric. The stator current or back EMF of these IPMSMs is not sensitive to eccentricity [16]. To diagnose the eccentricity of these IPMSMs by using stator current or back EMF, more instrumentation and complicated algorithms for signal processing are required [17]–[19]. Targeting this problem, Ma *et al.* [20] proposed a diagnostic method that only used fast Fourier transform (FFT) and the back EMF of each unit motor. Effective as this method is, additional cabling is required to connect windings of each unit motor to a data acquisition system, which makes this method again invasive.

(4) Other diagnostic signals other than the stray magnetic field. Vibration and acoustic signals [21] or torque ripples [22] can be used to non-invasively diagnose eccentricity but obtaining γ is impossible, an eccentricity parameter that helps describe the eccentricity more precisely and may expedite the repair process.

(5) Stray magnetic field (also called external magnetic field). From the above-reviewed categories of diagnostic approaches, a method that non-invasively diagnoses ε_{SE}, ε_{DE} and γ with an economical calculation cost is urgently needed for the extensive application of eccentricity diagnosis. To fill the research gap identified, a diagnostic method based on the open-circuit stray magnetic field is proposed in this paper. Compared with the aforementioned signals, the stray magnetic field has the advantage in determining γ as well as its non-invasive nature. As a result, the diagnostic methods based on it are gaining attention [12], [21]–[25]. Nevertheless, it has been observed that most of the existing papers have adopted the stray magnetic field to diagnose eccentricity on the induction motors and the electrically excited machines, rather than permanent magnetic motors.

It is well known that the permanent magnets in motors generate a great back EMF in windings at a high speed, and it may lead to catastrophic consequences once a short circuit of windings occurs even in the open-circuit condition [26]. This unique phenomenon of permanent magnetic motors, however, leads to a novel idea: using the open-circuit stray magnetic field for eccentricity diagnosis, which has not been studied before and may facilitate the offline inspection of motors. Although this idea seems to be practical, the theoretical basis of it is still weak because no existing literature provides an analytical model calculating the temporal and spatial distribution of the open-circuit stray magnetic field, especially with eccentricity. Analytical models in [27] and [28] can only calculate the amplitude of the stray magnetic field but no more information. Therefore, a more informative analytical model is needed.

Apart from diagnosing eccentricity in the open-circuit condition and establishing an analytical model, another gap is that no prototype motor is seen emulating eccentricity with all combinations of ε_{SE}, ε_{DE} and γ. Filling these gaps, this paper has the following main contribution and novelty:

1). An analytical model calculating the temporal and spatial distribution of the open-circuit stray magnetic field with eccentricity is proposed, which forms the basis of diagnosing the eccentricity of IPMSM by using the signal of the open-circuit stray magnetic field.

2). A non-invasive eccentricity diagnostic method is proposed, which can non-invasively diagnose ε_{SE}, ε_{DE}, and γ. This method does not require the connection of the tested motor and power supply, and its calculation cost is low.

3). An eccentricity prototype motor is invented, which can continuously emulate eccentricity with any ε_{SE}, ε_{DE}, and γ.

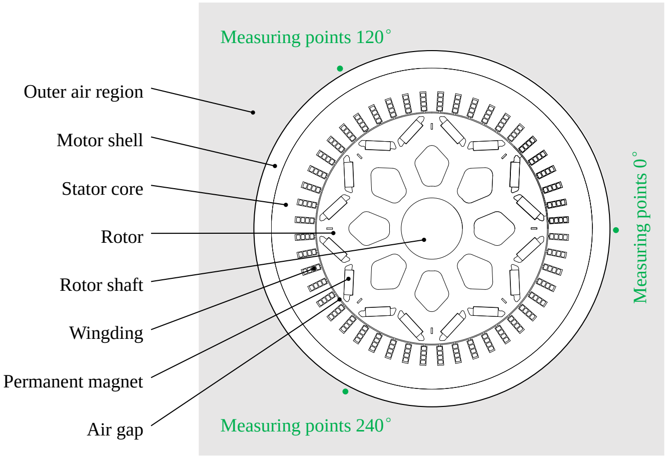

Fig. 2. Cross section of the 160-kW traction IPMSM for a typical EV.

TABLE I
STRUCTURAL PARAMETERS OF THE MOTOR

Parameter	Symbol	Quantity
Number of pole pairs	p	8
Number of slots	Q	48
Outer radius of the motor shell	R_{sho}	120 mm
Outer radius of the stator core	R_{so}	110 mm
Inner radius of the stator core	R_{si}	79.8 mm
Outer radius of the rotor	R_r	79.1 mm
Air-gap length with no eccentricity	g_0	0.7 mm
Axial length of the core	L_z	133 mm

Further, when the eccentricity adjustments of two ends are different, more complex eccentricity can be emulated. The prototype motor facilitates more research in this area.

This paper is organized as follows. In Section II, an analytical model of open-circuit radial stray magnetic flux density (RSMFD) is established. This model reveals the way eccentricity parameters influence the open-circuit RSMFD and forms the basis of the proposed diagnostic method. In Section III, data of the open-circuit RSMFD is obtained by experiments and then validates the analytical model. In Section IV, the data is used to establish an eccentricity diagnostic model. In Section V, the effectiveness of the proposed diagnostic model is validated against diagnosis results. Conclusions and future work are presented in Section VI.

II. THEORETICAL ANALYSIS

A. Model of Open-Circuit Air-gap Radial Magnetic Flux Density (RMFD) with Eccentricity

The rate power and speed of a typical traction IPMSM for EVs are 160 kW and 5100 rpm. Its cross section and structural parameters are shown in Fig. 2 and TABLE I, respectively. The pictures of the construction of the de-assembled motor are available in our previous work [29].

The temporal and spatial distribution of the air-gap length with ME can be expressed as (1), according to the geometric model of air-gap length with ME, as shown in Fig. 3.

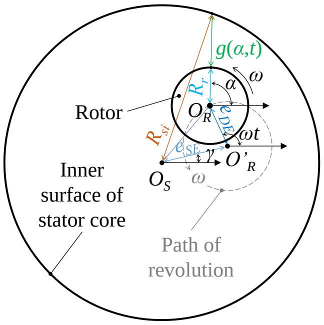

Fig. 3. Geometric model of air-gap length with ME.

$$g(\alpha,t) = \sqrt{{R_{Si}}^2 - {O_SO_R}^2\sin^2\left[\omega t - \alpha - \arccos\frac{e_{DE} + e_{SE}\cos(\omega t - \gamma)}{O_SO_R}\right]} - R_r - O_SO_R\cos\left[\omega t - \alpha \pm \arccos\frac{e_{DE} + e_{SE}\cos(\omega t - \gamma)}{O_SO_R}\right] \tag{1}$$

where t and α are time and spatial angle, respectively. "$\pm$" is "$-$", when $2k\pi \le \omega t - \gamma < (2k+1)\pi$, $k = 0,1,2,3\cdots$. Otherwise, "$\pm$" is "$+$", and

$$O_SO_R = \sqrt{{e_{SE}}^2 + {e_{DE}}^2 + 2e_{SE}e_{DE}\cos(\gamma - \omega t)} \ . \tag{2}$$

Apart from calculating the air-gap length with ME, (1) can also be used to calculate the air-gap length with SE or DE, if e_{SE} or e_{DE} is substituted with a very small value, e.g. 10^{-9} mm.

An Equivalent Magnetic Circuit (EMC) model calculating the spatial distribution of the open-circuit air-gap RMFD with no eccentricity (NE) can be established from [30]. Then, assuming that the slotting effect is neglected, by rotating the spatial distribution, the temporal and spatial distribution of the open-circuit air-gap RMFD with NE is obtained [31], which can be further expressed as Fourier series

$$B_r(\alpha,t) = \sum_{n=1,2,3\ldots}^{\infty}\left[a_n\cos(n\alpha + n\omega t) + b_n\sin(n\alpha + n\omega t)\right] \tag{3}$$

where ω is the angular speed of the rotor. n is the spatial order of the air-gap magnetic field. a_n and b_n are Fourier series coefficients.

The air-gap length in [30] is a constant number, and the corresponding magnetic reluctance R_g is also a constant number, which is expressed as

$$R_g = \frac{2g_0}{\mu_0 L_z (R_r + R_{si})} \tag{4}$$

where μ_0 is the permeability of air.

To calculate the open-circuit air-gap RMFD with eccentricity, g_0 in (4) is substituted by (1). Consequently, R_g turns into a function of both t and α, and then is written as R_{g_e}. Assuming that the magnetic saturation caused by eccentricity is neglected, relative permeance of eccentricity λ_e can be introduced

$$\lambda_e(\alpha,t) = R_{g\_e} / R_g \ . \tag{5}$$

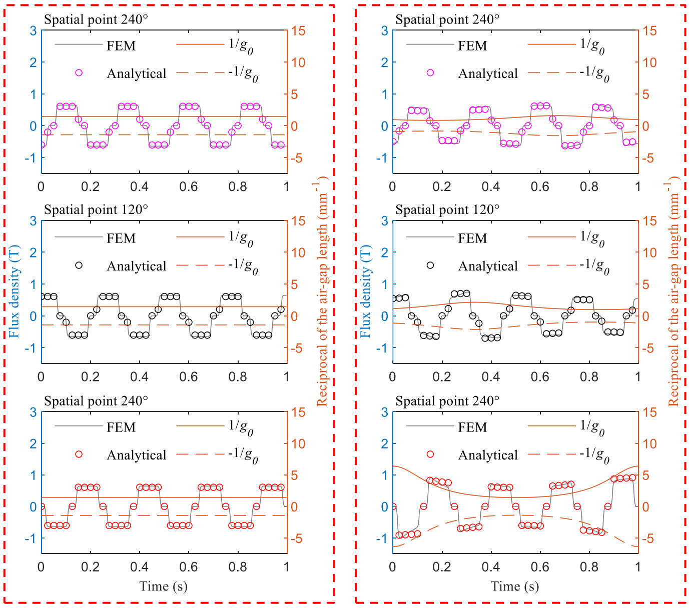

(a) (b)

Fig. 4. Temporal waveforms of the air-gap RMFD in different spatial points. (a) NE. (b) ME.

Then, the temporal and spatial distribution of open-circuit air-gap RMFD with eccentricity can be obtained

$$B_{r\_e}(\alpha,t)=B_r\lambda_e . \tag{6}$$

The software Ansys Maxwell is used as a finite element method (FEM) to validate the analytical results, as shown in Fig. 4. The temporal waveforms of the FEM and analytical calculations, of three spatial points, with NE and ME (ω=1 rad/s, ε_{SE}=0.4, ε_{DE}=0.4 and γ=20°), are compared. It can be found that the temporal waveforms of the air-gap RMFD in different spatial points change significantly if eccentricity occurs. Besides, the reciprocal of the air-gap length of the corresponding spatial points is also plotted in Fig. 4. It can be found that the reciprocal of the air-gap length has a similar variation trend as the open-circuit air-gap RMFD, which can also be deduced from (4)–(6).

B. Model of Open-circuit RSMFD with Eccentricity Based on Improved Attenuation Coefficients

In general, the amplitude of the open-circuit stray magnetic field is much smaller than its origin, the open-circuit air-gap magnetic field, due to attenuation phenomena. The ratio of the former amplitude to the later one is defined as the attenuation coefficient. Assuming that the eddy effect is neglected and only the air-gap magnetic field of spatial order p is considered, the attenuation coefficient can be obtained by solving Laplace's Equations and then expressed as [27]

$$K=\frac{2\left(\rho/R_{sho}\right)^{-p-1}}{\left(\mu_{rs}+1\right)\left(R_{si}/R_{so}\right)^{-p-1}-\left(\mu_{rs}-1\right)\left(R_{si}/R_{so}\right)^{p-1}} \tag{7}$$

where ρ is the distance between the measuring point and the center of the motor, and μ_{rs} is the relative permeability of the stator core.

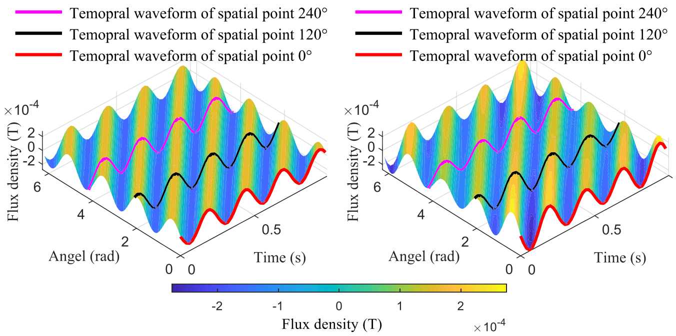

(a) (b)

Fig. 5. Temporal and spatial distribution of the open-circuit RSMFD. (a) NE. (b) ME.

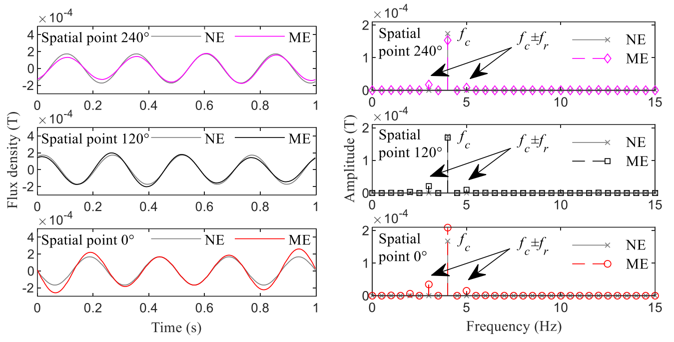

(a) (b)

Fig. 6. Temporal characteristics of the open-circuit RSMFD. (a) Waveforms. (b) Spectra.

Understandably, the correct temporal and spatial distribution of the open-circuit RSMFD cannot be obtained solely with (7), which is only used to calculate the amplitude in [27]. To further calculate waveforms, assuming that the air-gap magnetic field of all spatial orders are considered, improved attenuation coefficients can be generalized from (7) and expressed as

$$K_n=\frac{2\left(\rho/R_{sho}\right)^{-n-1}}{\left(\mu_{rs}+1\right)\left(R_{si}/R_{so}\right)^{-n-1}-\left(\mu_{rs}-1\right)\left(R_{si}/R_{so}\right)^{n-1}} . \tag{8}$$

By using (6) and (8), the temporal and spatial distribution of the open-circuit RSMFD with eccentricity is expressed as

$$B_{str\_e}(\alpha,t)=\lambda_e\sum_{n=1,2,3\ldots}^{\infty}K_n\left[a_n\cos\left(n\alpha+n\omega t\right)+b_n\sin\left(n\alpha+n\omega t\right)\right]. \tag{9}$$

From (9), the temporal and spatial distributions of the open-circuit RSMFD with NE and with ME (1 mm away from the outer surface of the motor shell, let ω=1 rad/s, ε_{SE}=0.4, ε_{DE}=0.4 and γ=20°) can be calculated, as shown in Fig. 5(a) and Fig. 5(b), respectively. By comparing these two subfigures, a conclusion can be reached that the temporal and spatial distribution of the open-circuit RSMFD changes significantly if eccentricity occurs. In these two subfigures, three curves in the curved surface are temporal waveforms of the open-circuit RSMFD of spatial points 240°, 120°, and 0°, where α=240°, 120°, and 0°, respectively; and the positions of the three measuring points are shown in Fig. 2.

By using FFT, the amplitude-frequency characteristics of these three waveforms are obtained, as shown in Fig. 6. It can be found that the amplitudes of the fundamental (with a frequency of f_c) and sideband harmonics around the

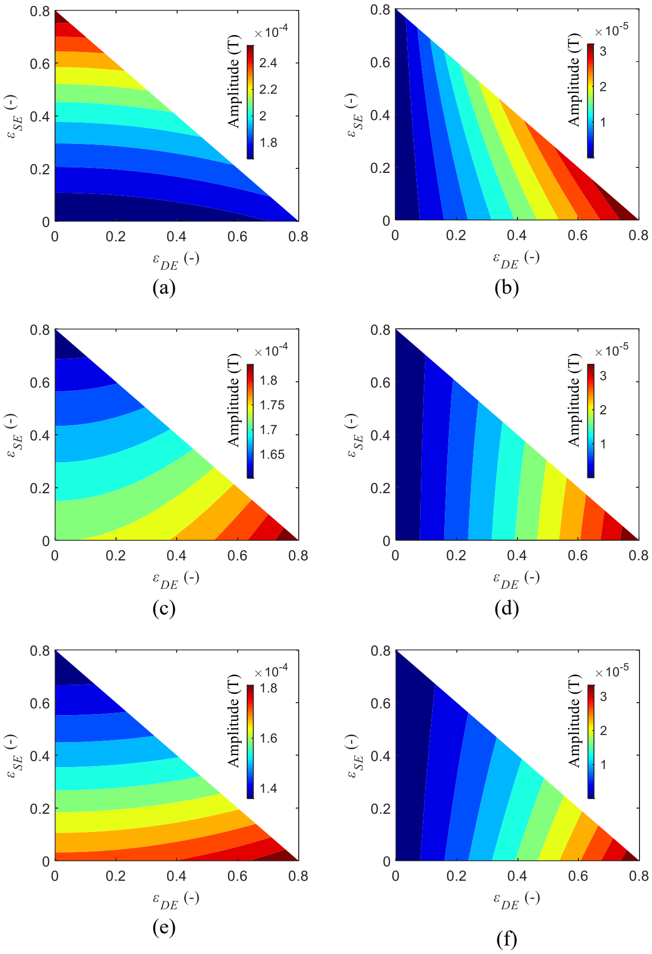

(a) (b)

(c) (d)

(e) (f)

Fig. 7. Amplitudes of the fundamental and mean amplitudes of the sideband harmonics of the open-circuit RSMFD with ME (analytical calculation results). (a) Amplitudes of the fundamental (α=0°). (b) Mean amplitudes of the sideband harmonics (α=0°). (c) Amplitudes of the fundamental (α=120°). (d) Mean amplitudes of the sideband harmonics (α=120°). (e) Amplitudes of the fundamental (α=240°). (f) Mean amplitudes of the sideband harmonics (α=240°).

fundamental (with frequencies of $f_c \pm f_r$, where f_r is the rotating frequency of rotor) change most significantly when ME occurs, compared with other harmonics. Besides, the patterns that these amplitudes of different spatial points change are also different. Therefore, these amplitudes are good indices to diagnose the eccentricity parameters.

C. Impact of Eccentricity Parameters on the Open-Circuit RSMFD

From the model of the open-circuit RSMFD with eccentricity, the change of the air-gap length when eccentricity occurs is the root cause of the change of the open-circuit RSMFD. Because $R_{si} \gg (e_{DE}+e_{SE})$, the radical expression in (1) can be simplified as R_{si}. Further, because $g_0 = (R_{si} - R_r)$, when only SE occurs, e_{DE}=0, (1) can be simplified as (10); when only DE occurs, e_{SE}=0, (1) can be simplified as (11).

$$g(\alpha,t) = g_0 - e_{SE}\cos(\gamma - \alpha) \tag{10}$$

$$g(\alpha,t) = g_0 - e_{DE}\cos(\omega t - \alpha) \tag{11}$$

From (10), it can be deduced that SE mainly changes the spatial orders of the air-gap length, and finally influences the amplitudes of the all harmonics of the open-circuit RSMFD of different measuring points; from (11), it can be deduced that DE mainly changes the temporal orders of the open-circuit RSMFD, and finally influences the amplitudes of sideband harmonics around the fundamental of different measuring points.

When ME occurs, however, (1) cannot be simplified to a concise form such as (10) or (11). Therefore, the pattern of the impact of eccentricity parameters on the air-gap length cannot be inferred directly from the expression. To investigate the pattern, accordingly, (9) is used to calculate the open-circuit RSMFD with different ε_{SE} and ε_{DE} (let γ=20°). Then, the amplitudes of the fundamental and the mean amplitudes of the sideband harmonics (with frequencies of $f_c \pm f_r$) of spatial points 240°, 120°, and 0° are obtained via FFT and then plotted, as shown in Fig. 7. It should be noted that the amplitudes of two sideband harmonics are not directly plotted here. Instead, the mean amplitudes of these two harmonics are calculated and plotted to avoid redundancy, since the two harmonics share similar characteristics when eccentricity parameters change.

From Fig. 7. It is found that: 1). Amplitudes of the fundamental of spatial points near γ are positively correlated to ε_{SE}, while amplitudes of the fundamentals of spatial points away from γ are negatively correlated to ε_{SE}. 2). Mean amplitudes of the sideband harmonics of all spatial points are positively correlated to ε_{DE}, and are not sensitive to ε_{SE}.

III. MEASURING EXPERIMENT OF OPEN-CIRCUIT RSMFD

A. Eccentricity Prototype Motor

An eccentricity prototype motor, which can continuously modify any eccentricity parameters, is proposed in this paper. The end-caps and the shell of the original motor are redesigned to achieve variable eccentricity parameters. The picture and the assembly drawing of the prototype motor are shown in Fig. 8(a). Since the adjusting mechanisms of both ends of the prototype are the same, only one end is described here. ε_{SE} is adjusted by a set of e_{SE} adjusting components on the end-cap, including a leadscrew and a reducer. A similar structure can be found in [2]. By rotating the leadscrew, the rotor can be pushed or pulled alongside the direction of the leadscrew to adjust SE.

The novelty of this prototype motor lies in the adjustment of ε_{DE} and γ. As shown in Fig. 8(b), ε_{DE} can be adjusted by changing the relative angle θ_{DE} between the inner and outer DE sleeves and secured by screws. θ_{DE} is calculated by (12) according to the geometric relation of the parameters in Fig. 8(c). γ can be adjusted by directly rotating the end-cap and secured by screws, as shown in Fig. 8(a).

$$\theta_{DE} = 2\arcsin\left(\frac{\varepsilon_{DE} g_0}{2e_0}\right) \tag{12}$$

where e_0 is the eccentricity length of the inner and outer DE sleeves, and it is smaller than $g_0/2$ to avoid rotor-to-stator rub.

In the existing literature, DE is achieved by an eccentric shaft housing [9] or a single eccentric sleeve [1], [12], which requires several additional eccentric components for different ε_{DE}s and can only adjust ε_{DE} step by step, whereas the proposed prototype is much more convenient. The proposed prototype

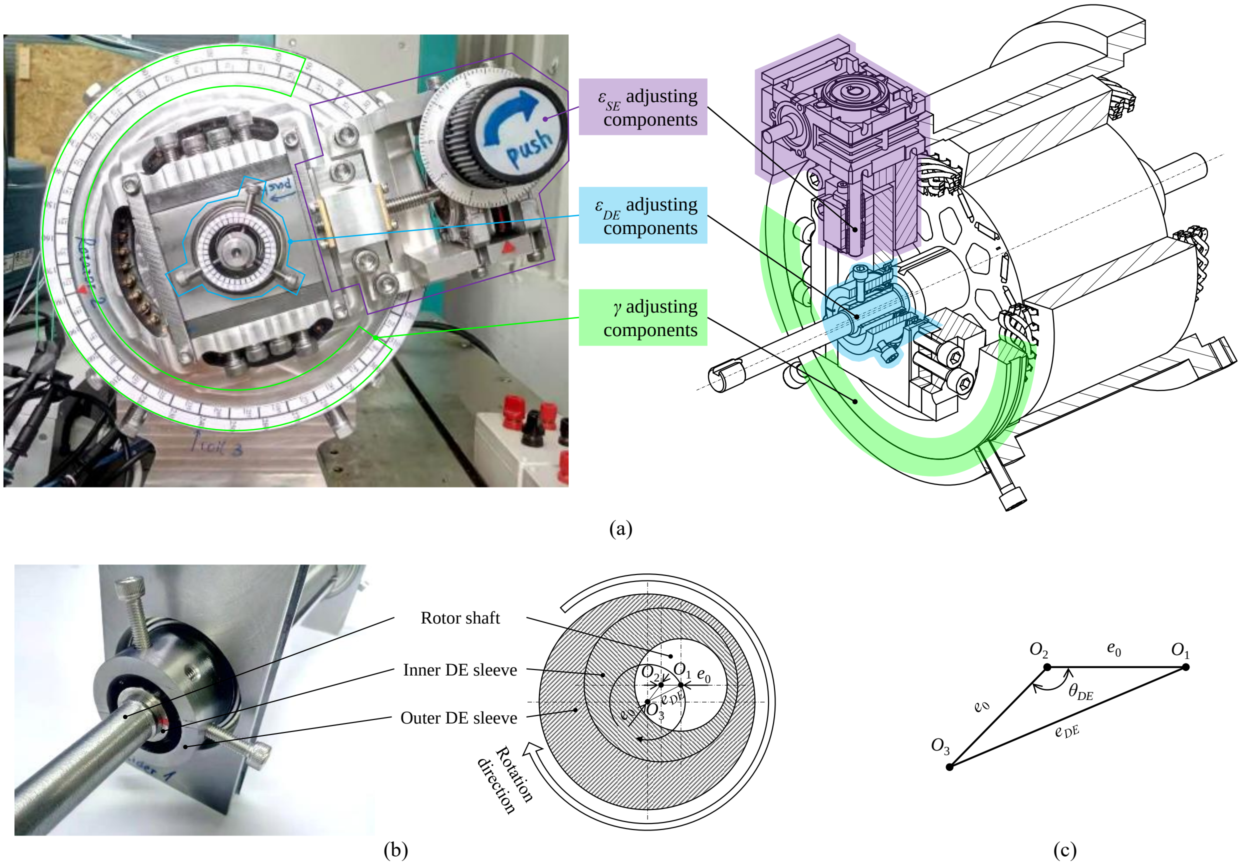

(a)

(b)

(c)

Fig. 8. Eccentricity prototype motor. (a) Picture and assembly drawing of the eccentricity prototype motor. (b) Picture and schematic of the ε_{DE} adjusting components. (c) Geometric schematic of the points O_1, O_2 and O_3.

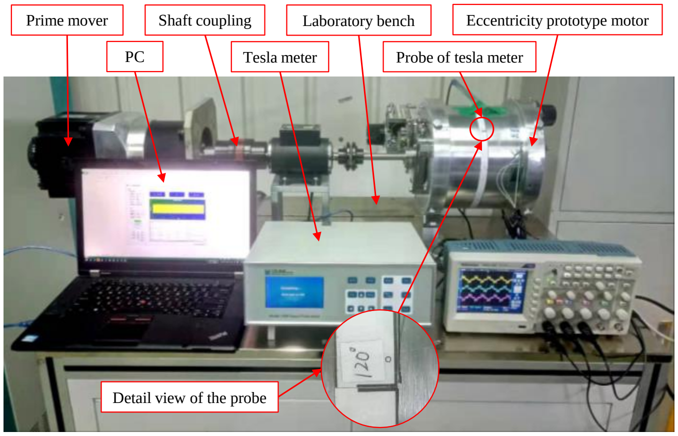

Fig. 9. Test rig for the eccentricity diagnosis of the IPMSM.

TABLE II

Settings of Eccentricity Ratios

ε_{SE} (-) / ε_{DE} (-)	0	0.1	0.2	0.3	0.4	0.5	0.6
0	**0**	**0.1**	**0.2**	**0.3**	**0.4**	**0.5**	**0.6**
0.1	**0.1**	**0.2**	**0.3**	**0.4**	**0.5**	**0.6**	
0.2	**0.2**	**0.3**	**0.4**	**0.5**	**0.6**		
0.3	**0.3**	**0.4**	**0.5**	**0.6**			
0.4	**0.4**	**0.5**	**0.6**				
0.5	**0.5**	**0.6**					
0.6	**0.6**						

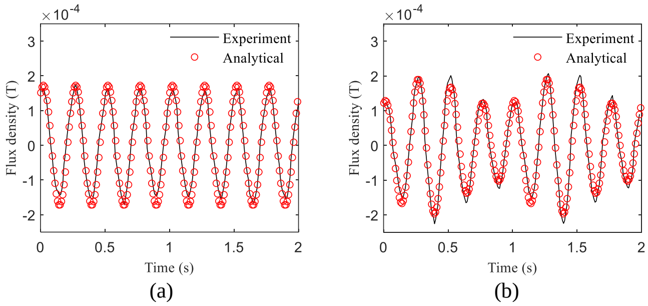

(a)

(b)

Fig. 10. Temporal waveforms of the open-circuit RSMFD of spatial points 120°. (a) NE (b) DE.

can set any ε_{DE} easily by changing θ_{DE} continuously, which greatly facilitates the research on the eccentricity of similar rotary machines.

B. Experimental Setup

A test rig is established to conduct the experiment, as shown in Fig. 9. An induction motor is used as the power source to motor the prototype motor, which is operated under the open-circuit condition. A tesla meter is used to non-invasively measure the open-circuit RSMFD of spatial points 240°, 120°, and 0° around the outer surface of the motor shell. The tesla meter, with a resolution of 1×10^{-7} T, is CH 1800 from CH-Magnetoelectricity Technology. Fig. 2 shows the angular positions of the measuring points. The probe of the tesla meter

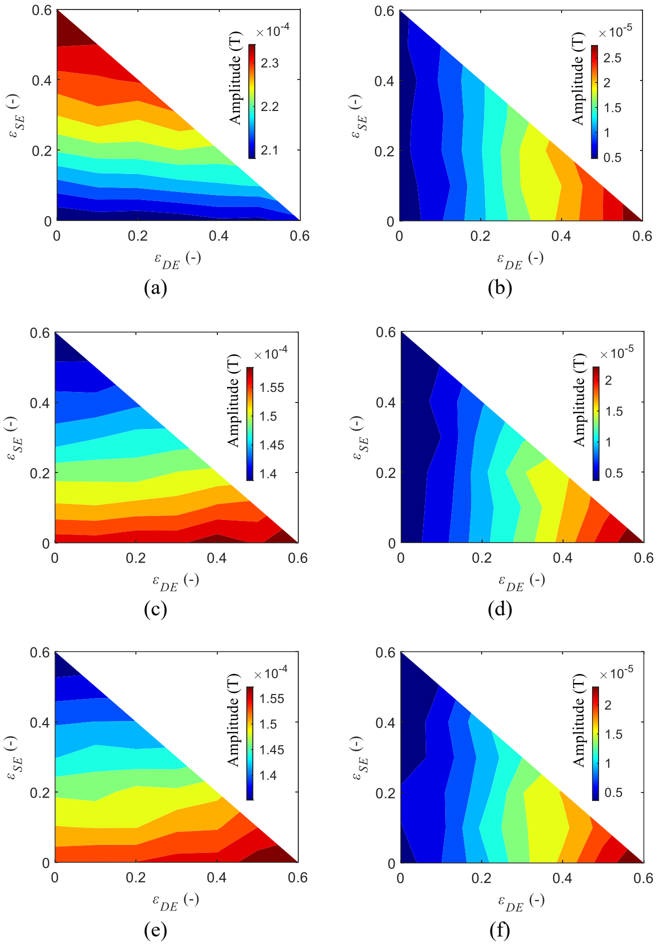

(a) (b) (c) (d) (e) (f)

Fig. 11. Mean values of amplitudes within the same eccentricity parameters of the fundamental and mean amplitudes of the sideband harmonics of the open-circuit RSMFD (experiment results). (a) Amplitudes of the fundamental (α=0°). (b) Mean amplitudes of the sideband harmonics (α=0°). (c) Amplitudes of the fundamental (α=120°). (d) Mean amplitudes of the sideband harmonics (α=120°). (e) Amplitudes of the fundamental (α=240°). (f) Mean amplitudes of the sideband harmonics (α=240°).

is placed in the axle-middle position of the prototype motor, as shown in Fig. 9, because the amplitude of the open-circuit RSMFD here is the highest [32]. The prototype motor maintains a motored speed of 24 rpm.

The RSMFD and the SCs voltage of the prototype motor are measured at different γ (240°, 120°, and 0°). Each set of data with the same γ contains 28 sets of combinations of ε_{SE} and ε_{DE}, as shown in TABLE II, where bold numbers are values of $\varepsilon_{SE}+\varepsilon_{DE}$, which are smaller than one to avoid rotor-to-stator rub. Regarding each combination of ε_{SE} and ε_{DE} with one γ, data of four rotor cycles is measured and recorded for further diagnosis. Each set of data of one rotor cycle contains three temporal waveforms of measuring points of 240°, 120°, and 0°. Consequently, $3\times28\times4\times3=1008$ sets of temporal waveforms are recorded in the experiment.

C. Validation of the Theoretical Analysis

Due to the significant amount of data recorded in the experiment, it is not straightforward to compare and visualize all of the data directly with the analytical calculation results. Therefore, temporal waveforms of the open-circuit RSMFD of spatial points 120° of the analytical model and the experiment are selected and compared in Fig. 10 to validate the theoretical analysis in Section II. Both the waveforms with NE and DE (ε_{DE}=0.6) are plotted, and a good agreement is achieved.

The amplitudes of all experiment waveforms are further calculated and discussed in Section IV.

IV. PROPOSED ECCENTRICITY DIAGNOSTIC METHOD

Based on the aforementioned impact pattern, the open-circuit RSMFD of a prototype motor with different eccentricity parameters can be selected as a diagnostic signal to establish an eccentricity diagnostic model. Then, by collecting the data of the diagnostic signal of motors under inspection and feeding them into a diagnostic model, the eccentricity parameters of the motors can be obtained.

A. Acquisition of the Training Data

The measuring points are spatially distributed points at 240°, 120°, and 0° around the motor, which have been described in Section III. By applying FFT, the amplitudes of the fundamental and mean amplitudes of the sideband harmonics of the experiment results are obtained. The mean values of the amplitudes with the same eccentricity parameters of four rotor cycles are calculated and plotted, as shown in Fig. 11. Fig. 7 and Fig. 11 show the same pattern, which also substantiates the theoretical analysis in Section II.

B. Establishment of the Diagnostic Model

Since the theoretical analysis has been done, which functions as the Feature Engineering, deep learning methods are not needed to establish the diagnostic model. Using the data in Fig. 11 as features, and corresponding eccentricity parameters as labels, a simple Back-Propagation Neural Network diagnostic model based on the open-circuit RSMFD is established [33]. Including the signal processing procedure FFT, the proposed diagnostic model is depicted in Fig. 12. Where, the numbers of hidden layers, input nodes, hidden nodes, and output nodes are 1, 6, 12, and 3, respectively. The input of the diagnosis model is amplitudes of the fundamental and mean amplitudes of the sideband harmonics of three measuring points, and the output are three eccentricity parameters, i.e., ε_{SE}, ε_{DE} and γ. The Min-Max normalization is used to scale the raw input data. The activation functions between the three layers are sigmoid and linear activation functions, respectively.

The Back-Propagation Neural Network diagnosis model is built in the software MATLAB and trained by a laptop with an i7-3840QM CPU and 16 G RAM. By using gradient descent, the training process takes about ten seconds.

C. Eccentricity Diagnosis

After the establishment of the diagnosis model, the diagnosis results of motors under inspection can be obtained by a similar way of establishing the diagnosis model, which is described in Fig. 12. The only difference is that the diagnostic signal comes from the motors under inspection rather than the eccentricity prototype motor.

Since the open-circuit RSMFD is used and its amplitude is quite small, the proposed method cannot be adopted as an in-line diagnostic method. Nonetheless, this method is suitable

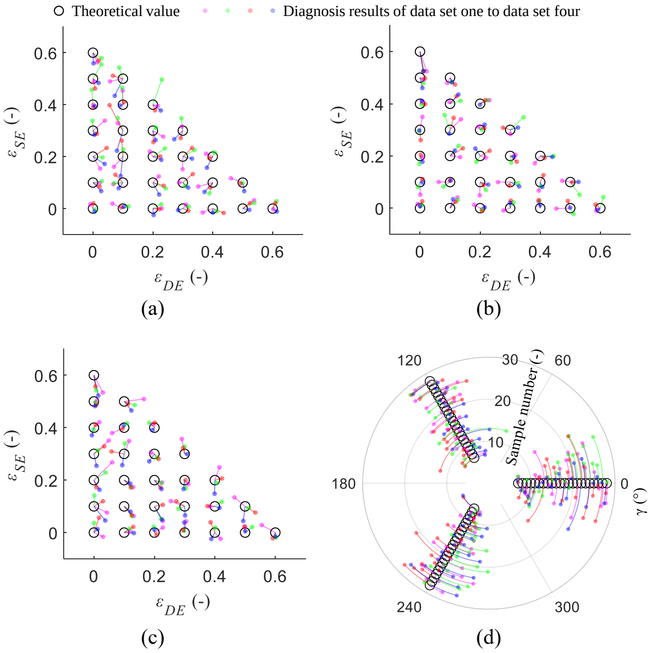

(a) (b) (c) (d)

Fig. 13. Diagnosis results of the proposed diagnostic model based on the open-circuit RSMFD. (a) Diagnosis results of ε_{SE} and ε_{DE} when γ=0°. (b) Diagnosis results of ε_{SE} and ε_{DE} when γ=120°. (c) Diagnosis results of ε_{SE} and ε_{DE} when γ=240°. (d) Diagnosis results of γ when $\varepsilon_{SE}\neq0$.

TABLE III

MEAN ABSOLUTE DIAGNOSTIC ERRORS

Item	Data set one	Data set two	Data set three	Data set four	Average
ε_{SE} (-)	0.0227	0.0247	0.0211	0.0238	0.0231
ε_{DE} (-)	0.0218	0.0157	0.0160	0.0133	0.0167
γ (°)	13.28	12.99	15.31	13.18	13.69

for the offline inspection of motor manufacturers. By checking every IPMSM after the manufacturing process, the initial eccentricity information of products can be obtained and the quality of products can be assessed. For the users of IPMSMs, such as automotive manufacturers, this method can also be used for Incoming Quality Control without additional process costs for suppliers or original equipment manufacturers (OEMs).

V. DIAGNOSIS RESULTS AND DISCUSSION

After the establishment of the diagnosis models, amplitudes of the fundamental and mean amplitudes of the sideband harmonics of four rotor cycles are fed into the diagnosis model to obtain diagnosis results, which are shown in Fig. 13. In Fig. 13, the data of four rotor cycles is named data set one to four; black circles denote theoretical values, i.e., the man-made eccentricity parameters of the corresponding data recorded; colored dots denote the diagnosis results of the data set one to four; diagnosis results and corresponding labels are connected with colored lines for visualization. It should be noticed that the diagnosis results, of which theoretical values $\varepsilon_{SE}=0$, are not plotted in Fig. 13(d) since γ theoretically does not exist when $\varepsilon_{SE}=0$. It can be found that nearly all of the diagnosis results have absolute errors of ε_{SE} and ε_{DE} less than 0.1, and absolute errors of γ less than 30°.

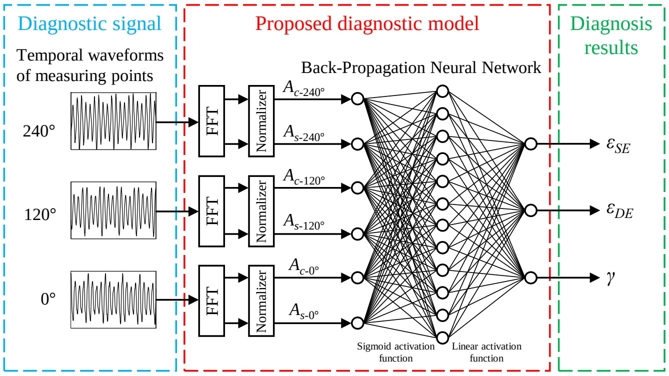

$A_{c\text{-}240°}$, $A_{c\text{-}120°}$ and $A_{c\text{-}0°}$ denote three amplitudes of the fundamental.
$A_{s\text{-}240°}$, $A_{s\text{-}120°}$ and $A_{s\text{-}0°}$ denote three mean amplitudes of the sideband harmonics.

Fig. 12. Schematic of the proposed diagnostic model.

Mean absolute errors of diagnosis results are shown in TABLE III. Average absolute errors of ε_{SE}, ε_{DE}, and γ are 0.0231, 0.0167, and 13.69°, respectively. As a comparison, the absolute errors of γ of diagnosis results are 5°–7° in [25]. Although the accuracy of the diagnosis results of γ of the proposed method seems to be lower than that in [25], it should also be noted that, in [25], only SE is studied, and four sensors are used (more sensors used, more accurate). Besides, in this paper, another similar diagnostic model based on a well-studied signal—SCs voltage is also established, in which only the diagnostic signal is different from the proposed diagnostic model. In fact, the diagnostic models based on the open-circuit RSMFD and the SCs voltage have a similar diagnostic accuracy. Therefore, a conclusion can be drawn that the accuracy of the proposed method reaches a state-of-the-art level.

VI. CONCLUSION AND FUTURE WORK

An eccentricity diagnostic method based on the open-circuit RSMFD is proposed in this paper. The basis of this method is formed by theoretical analysis of the analytical model, and the effectiveness of this method is validated by experimental data. This non-invasive method does not require the tested motor to be connected to the power supply, and only uses simple FFT to process raw signals. Consequently, this method is suitable for the offline inspection of motors manufacturers or other similar scenarios. The conclusions of this study are as follows:

1). Regarding the open-circuit RSMFD, amplitudes of the fundamental of spatial points near γ are positively correlated to ε_{SE}, while amplitudes of the fundamentals of spatial points away from γ are negatively correlated to ε_{SE}. Mean amplitudes of the sideband harmonics of all spatial points are positively correlated to ε_{DE}, and insensitive to ε_{SE}.

2). The accuracy of the proposed diagnostic method reaches a state-of-the-art level. The average absolute diagnostic errors of ε_{SE}, ε_{DE}, and γ are 0.0231, 0.0167, and 13.69°, respectively.

The further work of this paper lies in the case of mixed faults scenarios. The eccentricity fault diagnosis has been thoroughly studied in this paper, and it is handled as a regression problem. Most of the existing literature handled mixed faults diagnosis, like winding fault, demagnetization, together with eccentricity, as a classification problem. The future study can be carried out by combining the regression and the classification problems, which is more meaningful in the industry.

REFERENCES

[1] S. Nandi, T. C. Ilamparithi, S. B. Lee, and D. Hyun, "Detection of eccentricity faults in induction machines based on nameplate parameters," *IEEE Trans. Ind. Electron.*, vol. 58, no. 5, pp. 1673–1683, May 2011.

[2] Z. Q. Zhu, M. L. Mohd Jamil, and L. J. Wu, "Influence of slot and pole number combinations on unbalanced magnetic force in PM machines with diametrically asymmetric windings," *IEEE Trans. Ind. Appl.*, vol. 49, no. 1, pp. 19–30, Jan./Feb. 2013.

[3] S. Zuo, F. Lin, and W. Deng, "Impact of rotor eccentricity on electromagnetic vibration and noise of permanent magnet synchronous motor," *J. Vibroengineering*, vol. 20, no. 2, pp. 923–935, Mar. 2018.

[4] R. Takahata, S. Wakui, K. Miyata, K. Noma, and M. Senoo, "Influence of rotor eccentricity on vibration characteristics of permanent magnet synchronous motor," *IEEJ J. Ind. Appl.*, vol. 8, no. 3, pp. 558–565, 2019.

[5] Z. J. Liu, P. J. Zhang, S. He, and J. Huang, "A Review of Modeling and Diagnostic Techniques for Eccentricity Fault in Electric Machines," *Energies*, vol. 14, p. 4296, Jul. 2021.

[6] K.-T. Kim, K.-S. Kim, S.-M. Hwang, T.-J. Kim, and Y.-H. Jung, "Comparison of magnetic forces for IPM and SPM motor with rotor eccentricity," *IEEE Trans. Magn.*, vol. 37, no. 5, pp. 3448–3451, Sep. 2001.

[7] G. Mirzaeva and K. I. Saad, "Advanced diagnosis of rotor faults and eccentricity in induction motors based on internal flux measurement," *IEEE Trans. Ind. Appl.*, vol. 54, no. 3, pp. 2981–2991, May/Jun. 2018.

[8] G. Mirzaeva and K. I. Saad, "Advanced diagnosis of stator turn-to-turn faults and static eccentricity in induction motors based on internal flux measurement," *IEEE Trans. Ind. Appl.*, vol. 54, no. 4, pp. 3961–3970, Jul./Aug. 2018.

[9] Y. Da, X. Shi, and M. Krishnamurthy, "A new approach to fault diagnostics for permanent magnet synchronous machines using electromagnetic signature analysis," *IEEE Trans. Power Electron.*, vol. 28, no. 8, pp. 4104–4112, Aug. 2013.

[10] K. Kang, J. Song, C. Kan, S. Sung, and G. Jang, "Real-time detection of the dynamic eccentricity in permanent-magnet synchronous motors by monitoring speed and back EMF induced in an additional winding," *IEEE Trans. Ind. Electron.*, vol. 64, no. 9, pp. 7191–7200, Sep. 2017.

[11] H. Lasjerdi, Z. Nasiri-Gheidari, and F. Tootoonchian, "Static eccentricity fault diagnosis in wound-rotor resolvers," *IEEE Sensors J.*, vol. 21, no. 2, pp. 1424–1432, Jan. 2021.

[12] J. Shin, Y. Park and S. B. Lee, "Flux-based detection and classification of induction motor eccentricity, rotor cage, and load defects," *IEEE Trans. Ind. Appl.*, vol. 57, no. 3, pp. 2471–2480, May/Jun. 2021.

[13] H. F. Wang, Q. Lv, Y. Fang, Y. G. He, and X. H. Bao, "Detection of air-gap eccentricity in induction machines using multi-position magnetic field measurement approach," *Int. J. Appl. Electromagn. Mech*., vol. 47, no. 2, pp. 503–512, Feb. 2015.

[14] M. Petrinic, S. Tvoric, E. Plavec, and B. Zrakic, "Distinction of asymmetric load from eccentricity or synchronous electric generator winding fault using search coil measurements," *IEEE Trans. Ind. Appl.*, vol. 57, no. 5, pp. 4776–4785, Sep./Oct. 2021.

[15] J. Pons-Llinares, J. Antonino-Daviu, J. Roger-Folch, D. Moríñigo-Sotelo, and O. Duque-Pérez, "Mixed eccentricity diagnosis in inverter-fed induction motors via the adaptive slope transform of transient stator currents," *Mech. Syst. Signal Process.*, vol. 48, no. 1–2, pp. 423–435, Oct. 2014.

[16] Z. Q. Zhu, L. J. Wu, and M. L. M. Jamil, "Distortion of back-EMF and torque of PM brushless machines due to eccentricity," *IEEE Trans. Magn.*, vol. 49, no. 8, pp. 4927–4936, Aug. 2013.

[17] B. Ebrahimi, M. Roshtkhari, J. Faiz, and S. Khatami, "Advanced eccentricity fault recognition in permanent magnet synchronous motors using stator current signature analysis," *IEEE Trans. Ind. Electron.*, vol. 61, no. 4, pp. 2041–2052, Apr. 2014.

[18] Z. J. Liu, J. Huang, and B. N. Li, "Diagnosing and distinguishing rotor eccentricity from partial demagnetisation of interior PMSM based on fluctuation of high-frequency d-axis inductance and rotor flux," *IET Elect. Power Appl.*, vol. 11, no. 7, pp. 1265–1275, Aug. 2017.

[19] A. Aggarwal, I. M. Allafi, E. G. Strangas, and J. S. Agapiou, "Off-line detection of static eccentricity of PMSM robust to machine operating temperature and rotor position misalignment using incremental inductance approach," *IEEE Trans. Transport. Electrific*., vol. 7, no. 1 pp. 161–169, Mar. 2021.

[20] C. G. Ma, Y. J. Gao, M. Degano, Y. Y. Wang, J. G. Fang, C. Gerada, *et al*., "Eccentric position diagnosis of static eccentricity fault of external rotor permanent magnet synchronous motor as an in-wheel motor," *IET Elect. Power Appl.*, vol. 14, no. 11, pp. 2263–2272, Nov. 2020.

[21] E. T. Esfahani, S. Wang, and V. Sundararajan, "Multisensor wireless system for eccentricity and bearing fault detection in induction motors," *IEEE/ASME Trans. Mechatronics*, vol. 19, no. 3, pp. 818–826, Jun. 2014.

[22] Y. L. He, Z. J. Zhang, X. L. Wang, P. Gao, D. Gerada, C. Gerada, *et al*., "Impact of single and combined faults composed of rotor eccentricity and stator interturn short circuit on electromagnetic torque ripples in synchronous generator," *Complexity*, vol. 2020, pp. 1–21, Mar. 2020.

[23] I. Zamudio-Ramírez, R. A. Osornio-Ríos, J. A. Antonino-Daviu, and A. Quijano-Lopez, "Smart-sensor for the automatic detection of electromechanical faults in induction motors based on the transient stray flux analysis," *Sensors*, vol. 20, No. 5, p. 1477, Mar. 2020.

[24] H. Ehya, A. Nysveen, R. Nilssen, and Y. Liu, "Static and dynamic eccentricity fault diagnosis of large salient pole synchronous generators by means of external magnetic field," *IET Elect. Power Appl.*, vol. 15, no. 7, pp. 890–902, Jul. 2021.

[25] Y. L. He, Z. J. Zhang, W. Q. Tao, X. L. Wang, D. Gerada, C. Gerada, *et al*., "A new external search coil based method to detect detailed static air-gap eccentricity position in nonsalient pole synchronous generators," *IEEE Trans. Ind. Electron.*, vol. 68, no. 8, pp. 7535–7544, Aug. 2021.

[26] V. Gurusamy, E. Bostanci, C. Li, Y. Qi, and B. Akin, "A stray magnetic flux-based robust diagnosis method for detection and location of interturn short circuit fault in PMSM," *IEEE Trans. Instrum. Meas.*, vol. 70, pp. 1-11, 2021.

[27] R. Romary, D. Roger, and J. F. Brudny, "Analytical computation of an AC machine external magnetic field," *Eur. Phys. J., Appl. Phys.*, vol. 47, no. 3, Paper 31102, Sep. 2009.

[28] A. A. Adam, K. Gulez, and S. Koroglu, "Stray magnetic field distributed around a PMSM," *Turkish J. Electr. Eng. Comput. Sci.*, vol. 19, pp. 119–131, 2011.

[29] Y. S. An, C. G. Ma, N. Zhang, Y. Guo, M. Degano, C. Gerada, *et al*., "Calculation model of armature reaction magnetic field of interior permanent magnet synchronous motor with segmented skewed poles" *IEEE Trans. Energy Conver.*, 2021, DOI: 10.1109/TEC.2021.3123359.

[30] L. Zhu, S. Z. Jiang, Z. Q. Zhu, and C. C. Chan, "Analytical modeling of open-circuit air-gap field distributions in multisegment and multilayer interior permanent-magnet machines," *IEEE Trans. Magn.*, vol. 45, no. 8, pp. 3121–3130, Aug. 2009.

[31] C. G. Ma, J. J. Zhang, J. F. Wang, N. Yang, Q. H. Liu, S. G. Zuo, *et al.*, "Analytical model of open-circuit air-gap field distribution in interior permanent magnet machines based on magnetic equivalent circuit method and boundary conditions of Macroscopic Equations," *IEEE Trans. Magn.*, vol. 49, no. 3, pp. 1–9, Mar. 2021.

[32] Z. Liu, G. Y. Tian, W. P. Cao, X. W. Dai, B. Shaw, and R. Lambert, "Non-invasive load monitoring of induction motor drives using magnetic flux sensors," *IET Power Electron.*, vol. 10, no. 2, pp. 189–195, Feb. 2017.

[33] C.G. Ma, Q. Li, Q.H. Liu, D.F. Wang, J.J. Gao, H.Y. Tang, *et al.*, "Sound quality evaluation of noise of hub permanent-magnet synchronous motors for electric vehicles," *IEEE Trans. Ind. Electron.*, vol.63, no.9, pp. 5663–5673, Sep. 2016.

Conggan Ma (M'14) was born in Sichuan, China, in 1987. He received the B.S.E. and Ph.D. degrees in automotive engineering from Tongji University, Shanghai, China, in 2010 and 2014, respectively.

Since 2019, he has been a professor with the Automotive Engineering College, Harbin Institute of Technology-Weihai, Weihai, China, where he was an associate professor from 2014 to 2019. His research interests include vehicle system dynamics and control, vehicle vibration and noise control, and vibration and noise of electrical machines.

Professor Ma is a senior member of IEEE, a commissioner of the Youth Work Committee of the China Society of Automotive Engineers, a senior member of the Chinese Society for Vibration and Engineering, a member of IEEE Vehicular Technology Society, a member of the Chinese Society of Theoretical and Applied Mechanics, and a member of the China Society of Automotive Engineers.

Jiaming Li received the B.S.E. and M.S.E. degrees in vehicle engineering from Harbin Institute of Technology-Weihai, Weihai, China, in 2015 and 2021, respectively. He was a quality engineer of FAW-Volkswagen Automotive Co. Ltd from 2015 to 2018. He is currently working toward the Ph.D. degree in Electromechanical Engineering, in the Faculty of Science and Technology at the University of Macau.

His research interests include fault diagnosis of electromechanical equipment.

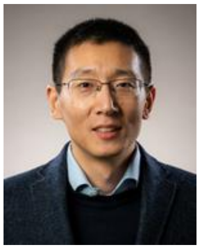

Nic Zhang was born in Shandong, China, in 1986. He received his BEng degree in Vehicle Engineering from Tongji University of Shanghai, China in 2010, and his MSc in Automotive Engineering in 2011 and PhD in Mechanical Engineering in 2016 from University of Bath, UK. He is lecturer in Data Science and Artificial Intelligence at University of Bath, UK.

He has a wide research interest in automotive powertrain systems and automated driving systems. He has a wide range of industry experience through employment with Schaeffler Group, FEV GmbH and Jaguar Land Rover and various engineering consultancy projects for Ford Motors, Cummins, Honeywell, BorgWarner, etc.

Feifei Bu (M’11) was born in Maanshan, China, in 1984. He received the B.S. degree in electrical engineering from Anhui University of Technology, Maanshan, China, in 2006, and the Ph.D. degree (master–doctorate program) in electrical engineering from Nanjing University of Aeronautics and Astronautics, Nanjing, China, in 2014.

He joined the faculty of the Department of Electrical Engineering, NUAA, in 2014, where he is currently an Associate Professor. His research interests include power electronics and electrical machines for standalone power systems, renewable energy generating systems, electric vehicle driving systems, etc.

Zhixin Yang (M'14) obtained his Ph.D. degree in industrial engineering and engineering management from the Hong Kong University of Science and Technology, Hong Kong, China, in 2000.

He is currently an Associate Professor with the State Key Laboratory of Internet of Things for Smart City and the Department of Electromechanical Engineering, University of Macau, Macau, China. His research interests include prognostic health management of electromechanical systems, computer vision based robotics, intelligent safety monitoring and maintenance.